

## REPORT DOCUMENTATION PAGE

AFRL-SR-AR-TR-04-

0460

The public reporting burden for this collection of information is estimated to average 1 hour per response, including 1 gathering and maintaining the data needed, and completing and reviewing the collection of information. Send comment of information, including suggestions for reducing the burden, to Department of Defense, Washington Headquarter (0704-0188), 1215 Jefferson Davis Highway, Suite 1204, Arlington, VA 22202-4302. Respondents should be aware subject to any penalty for failing to comply with a collection of information if it does not display a currently valid OMB control number.

**PLEASE DO NOT RETURN YOUR FORM TO THE ABOVE ADDRESS.**

1. REPORT DATE (DD-MM-YYYY) 23082004			2. REPORT TYPE FINAL REPORT		3. DATES COVERED (From - To) 1 May 2003 - 30 Apr 2004	
4. TITLE AND SUBTITLE Visualization of Flow Control Devices (VGJs) for Low Pressure Turbine Separation Control Using Stereo PIV					5a. CONTRACT NUMBER	
					5b. GRANT NUMBER F49620-03-1-0280	
					5c. PROGRAM ELEMENT NUMBER	
6. AUTHOR(S) DR JEFFREY P BONS					5d. PROJECT NUMBER	
					5e. TASK NUMBER	
					5f. WORK UNIT NUMBER	
7. PERFORMING ORGANIZATION NAME(S) AND ADDRESS(ES) Department of Mechanical Engineering Brigham Young University Provo Utah					8. PERFORMING ORGANIZATION REPORT NUMBER	
9. SPONSORING/MONITORING AGENCY NAME(S) AND ADDRESS(ES) USAF/AFRL AFOSR 801 N. Randolph Street Arlington VA 22203 N A					10. SPONSOR/MONITOR'S ACRONYM(S) AFOSR	
					11. SPONSOR/MONITOR'S REPORT NUMBER(S)	
12. DISTRIBUTION/AVAILABILITY STATEMENT Distribution Statement A. Approved for public release; distribution is unlimited.						
13. SUPPLEMENTARY NOTES 20040914 009						
14. ABSTRACT An AFOSR-sponsored collaborative effort in low-pressure turbine (LPT) flow control is currently underway to capitalize on recent laboratory successes using vortex generating jets (VGJs). AFRL/PRTT, the University of Arizona, and Brigham Young University (BYU) are all players in this effort to enhance the understanding of the effect of VGJs on separating LPT boundary layers. AFRL/PRTT has the design task (under Drs. Richard Rivir and Rolf Sondergaard) to integrate flow control strategies into the Air Force's jet engine inventory. To make the transition of VGJs from the laboratory to the design process will require a greatly improved understanding of the fundamental physics, so that accurate models can be developed and incorporated into LPT design codes. Dr. Hermann Fasel (University of Arizona) has an AFOSR grant to develop computational models as building blocks for this design integration process. The necessary experimental data to validate these models is being obtained from wind tunnel testing at BYU (Dr. Jeffrey Bons as PI).						
15. SUBJECT TERMS						
16. SECURITY CLASSIFICATION OF: a. REPORT U b. ABSTRACT U c. THIS PAGE U			17. LIMITATION OF ABSTRACT UU	18. NUMBER OF PAGES 17	19a. NAME OF RESPONSIBLE PERSON 19b. TELEPHONE NUMBER (Include area code)	

## DURIP GRANT FINAL REPORT

**Submitted To:** Dr. Thomas Beutner, AFOSR/NA

**DURIP Grant #:** F49620-03-1-0280

**Funding Level:** \$117,178

**Title:** Visualization of Flow Control Devices (VGJs) for Low Pressure Turbine Separation Control using Stereo PIV

**Principal Investigator:** Dr. Jeffrey P. Bons, Brigham Young University

### **Abstract**

An AFOSR-sponsored collaborative effort in low-pressure turbine (LPT) flow control is currently underway to capitalize on recent laboratory successes using vortex generating jets (VGJs). AFRL/PRTT, the University of Arizona, and Brigham Young University (BYU) are all players in this effort to enhance the understanding of the effect of VGJs on separating LPT boundary layers. AFRL/PRTT has the design task (under Drs. Richard Rivir and Rolf Sondergaard) to integrate flow control strategies into the Air Force's jet engine inventory. To make the transition of VGJs from the laboratory to the design process will require a greatly improved understanding of the fundamental physics, so that accurate models can be developed and incorporated into LPT design codes. Dr. Hermann Fasel (University of Arizona) has an AFOSR grant to develop computational models as building blocks for this design integration process. The necessary experimental data to validate these models is being obtained from wind tunnel testing at BYU (Dr. Jeffrey Bons as PI).

BYU has constructed a VGJ research wind tunnel with the capability to independently control both streamwise pressure gradient and surface curvature. These two parameters are critical to accurately model the complex jet/boundary layer interaction in the LPT. This DURIP grant was used to purchase a stereo-PIV flow diagnostic system. This system complements existing one and two-component hot-wire anemometry which is used to make time-averaged and time-resolved velocity measurements. Stereo-PIV provides the capability to more efficiently map large regions of the flowfield and obtain the third (out of plane) component of velocity. It also allows the detailed study of pulsed VGJ actuation. The PIV system greatly enhances both the quantity and quality of data provided for CFD validation. This report documents the use of the PIV system in support of this important AFOSR research initiative.

### **Background and Objectives of AFOSR-funded VGJ Research**

During high altitude cruise, the operating Reynolds number for the low-pressure turbine (LPT) in an aircraft gas turbine engine can drop below 25,000. This low Reynolds number condition is particularly acute in the class of small gas turbine engines used in many high altitude air vehicles. At these low Reynolds numbers, the boundary layers on the LPT blades are susceptible to flow separation near the aft portion of the blade suction surface, with associated loss increase and performance drop. Sondergaard et al. (2001) have measured a nearly 300% increase in loss coefficient at Reynolds numbers below 50,000 compared to the loss coefficient at higher Reynolds numbers (Figure 1). Similar results have been repeated by other researchers on full-scale engines (e.g. Sharma et al., 1998, and Matsunuma et al., 1998 and 1999). Though the exact Reynolds number at which separation related losses become significant is machine specific, the increased loss inevitably translates to a significant decrease in turbine efficiency at these operating conditions (measured values have been as much as a six point loss in component efficiency for the AE3007H [Helton, 1997], a small high altitude engine).

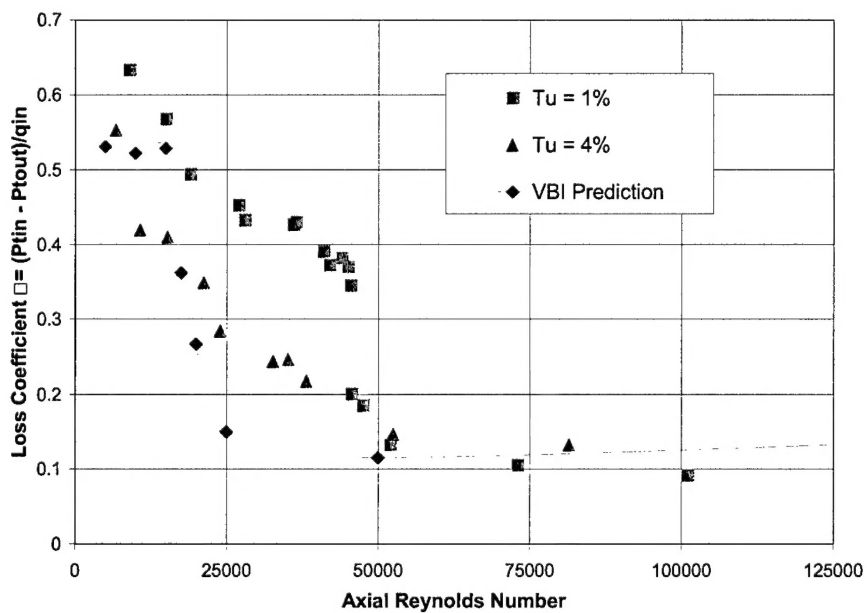


Figure 1: Loss coefficient  $\gamma$  vs. inlet Reynolds number. AFRL/PRTT Pak-B low speed cascade facility.

Tu = 1%, Tu = 4%, and VBI (CFD) prediction.

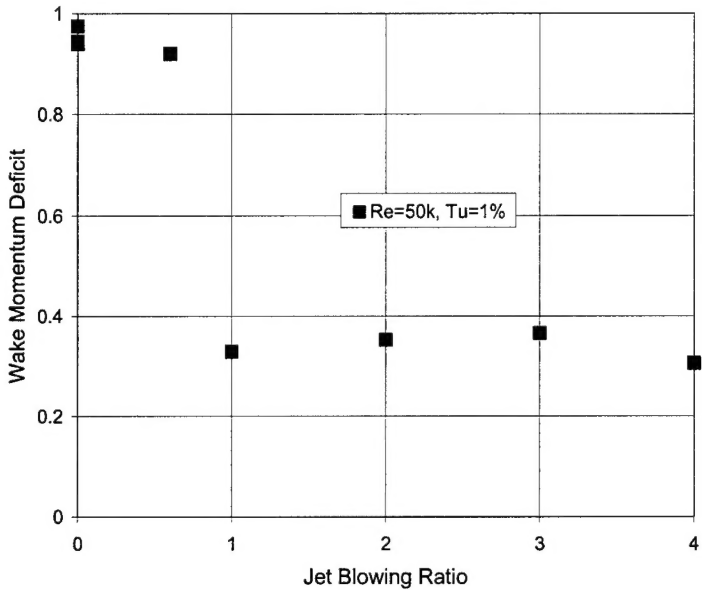


Figure 2: Wake Momentum Deficit vs. Jet Blowing Ratio (B). Data from AFRL/PRTT Pak-B low speed cascade facility with low turbulence and  $Re = 50,000$ .

Experiments using vortex generator jets (VGJs) on the LPT suction surface, conducted in AFRL's low-speed cascade at WPAFB (Bons et al., 1999), have demonstrated 25-65% reductions in separation losses at low Reynolds numbers (figure 2). The VGJs were configured with a 30 degree pitch angle and 90 degree skew angle to the near wall flow direction (figure 3). In this skew configuration, the VGJ creates a horseshoe vortex pair with one very strong leg accompanied by a weak leg of opposite sign. The result is a single, dominant, slowly-decaying streamwise vortex that energizes the separating boundary layer by effectively bringing high momentum freestream fluid down near the wall.

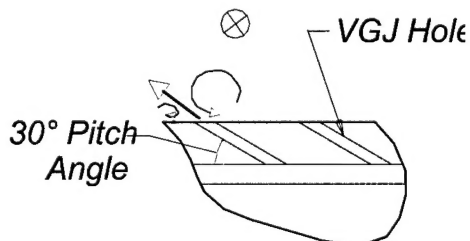


Figure 3: Schematic of VGJ hole geometry and vortex generation. (Main Flow is into page.)

The well-documented success of VGJs at correcting off-design (low  $Re$ ) separation deficiencies of an existing LPT airfoil has led to the consideration of broader applications for VGJs. In their most recent study (Sondergaard et al. 2002), the blade pitch (spacing) of an existing linear cascade (which operated without suction surface separation at design  $Re$ ) was increased at constant axial chord. This effectively reduced the cascade solidity and produced massive suction surface separation at design conditions due to

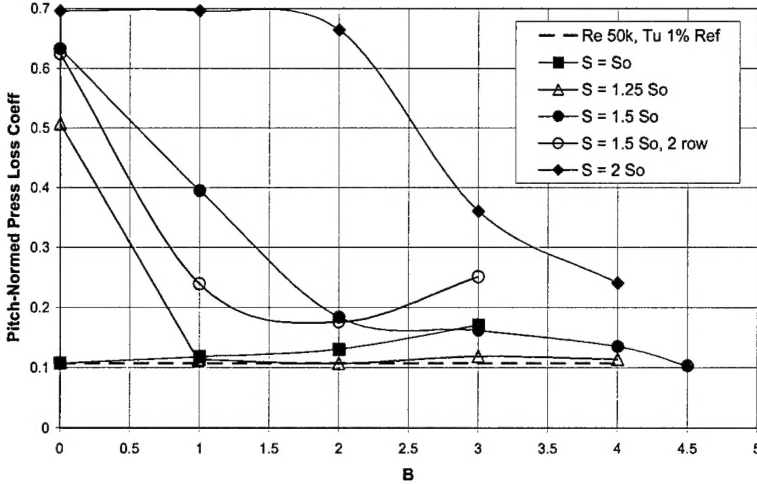


Figure 4: Wake pressure loss coefficient vs. blowing ratio B. Reynolds number 50,000. 1% Turbulence. VGJ injection at 45% Cx (45% and 63% injection for “2 row”). Four pitch spacings (S).

the large uncovered turning (with a six-fold increase in losses). Then by strategically incorporating VGJs on the blade suction surface, the pitch-averaged blade losses were reduced down to the standard pitch level (Figure 4). The end result was equivalent cascade performance with up to 50% fewer blades. This proof-of-concept demonstrated the potential to design highly-loaded, compact, low pressure turbines with integrated flow control.

The critical science that would enable this new design innovation to be implemented in a real engine is a full understanding of the effect of VGJs on a separating boundary layer. Once the physics of this interaction is understood, models could be developed and incorporated into existing design codes. Unfortunately, VGJs create an extremely complicated three dimensional flow, with vortices and multiple turbulent shear layers. For a research effort to be successful, it must skillfully integrate experimental measurement, computational modeling, and analytical design studies. Such is the goal of this combined AFRL–University of Arizona–BYU effort. AFOSR/NA has sponsored Drs. Richard Rivir and Rolf Sondergaard through their design task to explore opportunities for LPT enhanced design using integrated VGJs. In addition, AFOSR has funded a computational effort directed by Dr. Hermann Fasel at the University of Arizona to explore separation control in the LPT environment. BYU’s critical role is to obtain quality experimental data for model guidance and validation (research grant #FA 9550-04-1-0024).

#### Role of Stereo PIV System in Experimental Effort at BYU

Testing is being conducted in a low-speed turbine cascade facility at Brigham Young University (Figure 5). The facility has the flexibility to independently vary streamwise pressure gradient and wall curvature, two of the critical features affecting LPT boundary layer separation. The capability to control pressure gradient and wall curvature independently is essential to creating a design tool suitable for application to arbitrary LPT designs. A 3-axis traverse system mounted atop the tunnel is used to make one

and two- component velocity measurements at various planes downstream of the VGJs. The traverse is affixed to a rotary table to allow traverses normal to an arbitrary wall curvature.

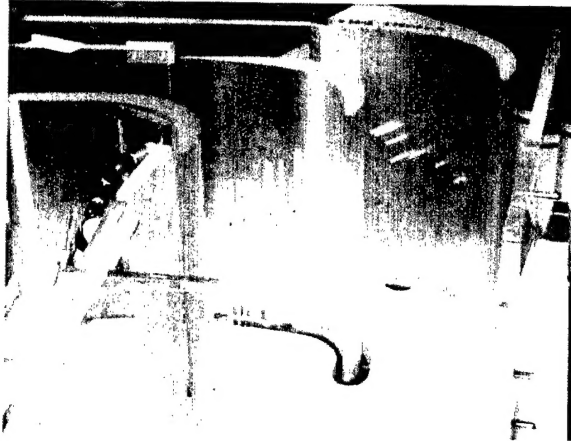


Figure 5: Low-speed cascade facility at BYU.

Two-component split film anemometry has allowed simultaneous measurement of the streamwise and wall-normal mean velocity components as well as turbulence quantities and Reynolds' stresses. Figure 6 provides an example of data available from 2-component cascade measurements (Eldredge and Bons, 2004). The VGJ jet evolution is clearly noted, with vertical flows providing evidence of vertical motion.

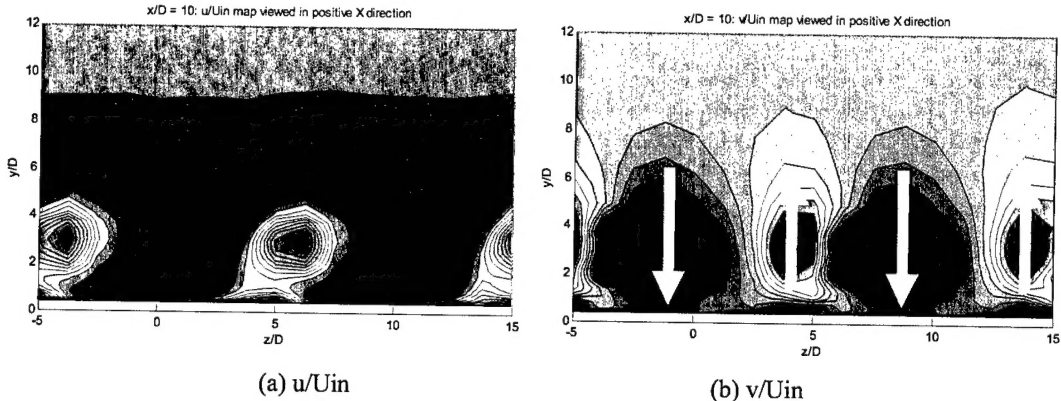


Figure 6: Streamwise (u) and wall-normal (v) velocity data at  $x/D = 10$  with  $B = 4$ .  $Re = 25,000$ .

Stereo-PIV compensates for two inherent shortcomings of 1 and 2-component hot-wire measurements: the lack of the 3<sup>rd</sup> velocity component and the tedious nature of point-by-point diagnostics. The BYU wind tunnel was constructed with maximum optical accessibility, both through the flexible outer wall and the top and bottom rigid walls. Laser light sheets in both the x-y and x-z planes are possible ( $x$  = streamwise,  $y$  = wall normal,  $z$  = spanwise), with imaging from CCD cameras in an orthogonal plane. This allows full interrogation of the VGJ-induced vortices and their interaction with the separation zone, to include the out-of-plane velocity component. Time accurate full-field data over the entire development length of the jets allows the study of pulsed VGJs and their interaction with a separating boundary layer.

## Research to date with PIV

Experiments were performed on a flat plate test section (Figure 7) with and without an imposed streamwise pressure gradient (Figure 8). A boundary layer bleed is employed at the leading edge to create a new, laminar boundary layer. There are two rows of 4mm diameter ( $d$ ) cylindrical VGJ holes: vertical holes aligned normal to the freestream direction, and angled holes with  $30^\circ$  pitch and  $90^\circ$  skew angles. The holes are placed approximately 10 diameters apart at 0.36m and 0.375m from the boundary layer bleed (for the angled and normal rows, respectively).

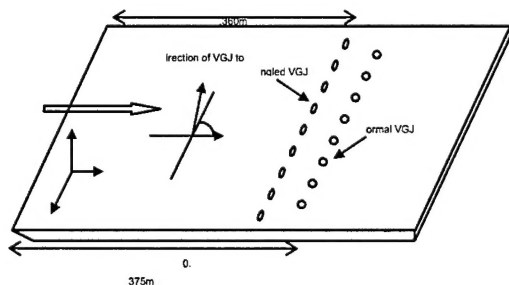


Figure 7: Flat Plate Test Section Schematic

To create a streamwise pressure gradient without modifying the wall curvature, a wedge was inserted into the wall opposite the flat plate. Suction was applied near the trailing edge of the wedge to insure proper diffusion of the main flow and facilitate separation on the flat plate test section. The wedge and its position with respect to the area of data collection are shown in Figure 8.

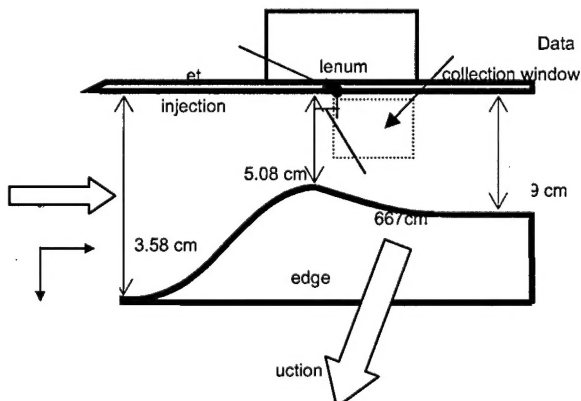


Figure 8: Flat Plate with Applied Pressure Gradient Schematic

Three dimensional flow measurements were made using the LaVision 3 component stereo PIV system purchased under this DURIP grant. This system was mounted on a 3-axis traverse located below the transparent acrylic test section to enable a full mapping of the flow field. An Nd:YAG laser illuminates the flow field with a light sheet approximately 1 mm in thickness. The flow is seeded with oil ( $C_{26}H_{50}O_4$ ) particles that are  $1-2\mu\text{m}$  in diameter. Images were recorded by two digital cameras with a resolution of 1376 by 1040 pixels.

To collect the data, the laser sheet was oriented in the x-y plane. Forty separate images at each  $z$  location were recorded, processed, and averaged. The pulsed jet measurements were phase-locked with the jet forcing, while the steady jet measurements were taken at an internal framing rate of 9.9 Hz. The use of two cameras (stereo PIV) allowed the measurement of  $u$ ,  $v$ , and  $w$  components of velocity in each box. This procedure was repeated at increments of 2mm in  $z$  in order to generate a three-dimensional block of velocity data. Vorticity components were then calculated from this data block using centered differences to approximate the velocity gradients.

### **Flat Plate, No Streamwise Pressure Gradient, Steady Jets**

For the steady jet cases, the constant freestream velocity ( $U_\infty$ ) was set so that the momentum thickness Reynolds number ( $Re_\theta$ ) at the VGJ location matched that used by Eldredge and Bons in their cascade study ( $Re_\theta \approx 150$ ). The steady jet blowing ratio ( $B$ =mean jet velocity divided by local freestream velocity) was set to a value of 2 since this was the lowest mass flow required for effective control in the study by Bons et al..

#### *Normal Injection*

Contour maps of streamwise and wall-normal velocity and the out of plane (streamwise) vorticity, plotted in  $z$ - $y$  planes at 10 diameters downstream from the jet injection

point, are shown in Figure 9. Velocities are normalized by  $U_\infty$  and data was taken over two hole pitches. The reader is referred to Figure 7 for the orientation of the Cartesian axes.  $x/d = 0$  is at the center line of the hole row,  $y/d = 0$  is at the wall, and  $z/d = 0$  is at the center of the hole.

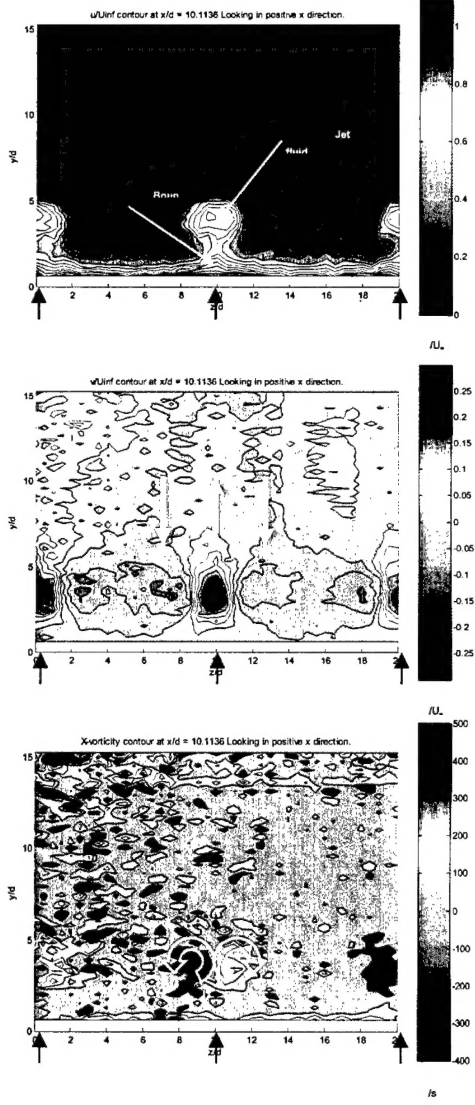


Figure 9: Streamwise and wall-normal velocity and out-of-plane (streamwise) vorticity contour maps showing vortex development at  $x/d=10$ . Black arrows indicate jet injection points. Steady, normal jet injection into zero pressure gradient with  $B=2$ .

Several important characteristics of the flow are evident from Figure 9. First, the lobes of low  $u$ -velocity fluid denote the position of the jet fluid which is injected with no streamwise momentum. This low velocity lobe gradually moves out from the wall as it travels

downstream, ultimately reaching a maximum  $y/d$  position of 4.5 (wall distance to the center of the lobe) at  $x/d=20$ . The jet trajectory is evident in the  $x$ - $y$  plane of streamwise vorticity shown in Figure 4. Since there is zero skew to the injection, the jet remains at the same  $z$  position throughout its trajectory (Figure 10).

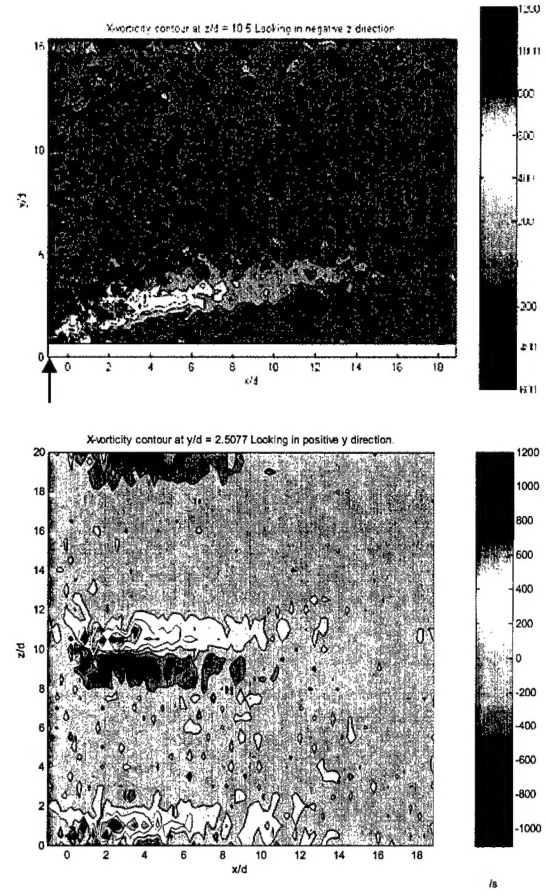


Figure 10: Streamwise vorticity contours shown in the  $xy$  (at  $z/d=10.5$ )  $xz$  (at  $y/d=2.5$ ) planes. Steady, normal jet injection into zero pressure gradient with  $B = 2$ .

Likewise observed from Figure 9 is the development of streamwise vortices. The  $v/U_\infty$  contour plot shows that these vortices develop as fluid is forced outward normally from the wall at the jet injection point and then cycled back towards the wall on both sides. This effect is promulgated downstream as the double vortex grows in size while decreasing in magnitude. After traveling 15 diameters downstream, the magnitude of the vorticity is reduced by 75% (see  $x$ - $z$  plot of streamwise vortices in Figure 10).

### Angled Injection

Similar results were obtained for the angled jets. Figure 11 again shows streamwise and wall-normal velocity and out of plane (streamwise) vorticity contours in the  $z-y$  plane at the same downstream location of  $x/d=10$ . Figure 12 shows the corresponding  $x-y$  and  $x-z$  planes of streamwise vorticity. The velocity is again normalized by the freestream value.

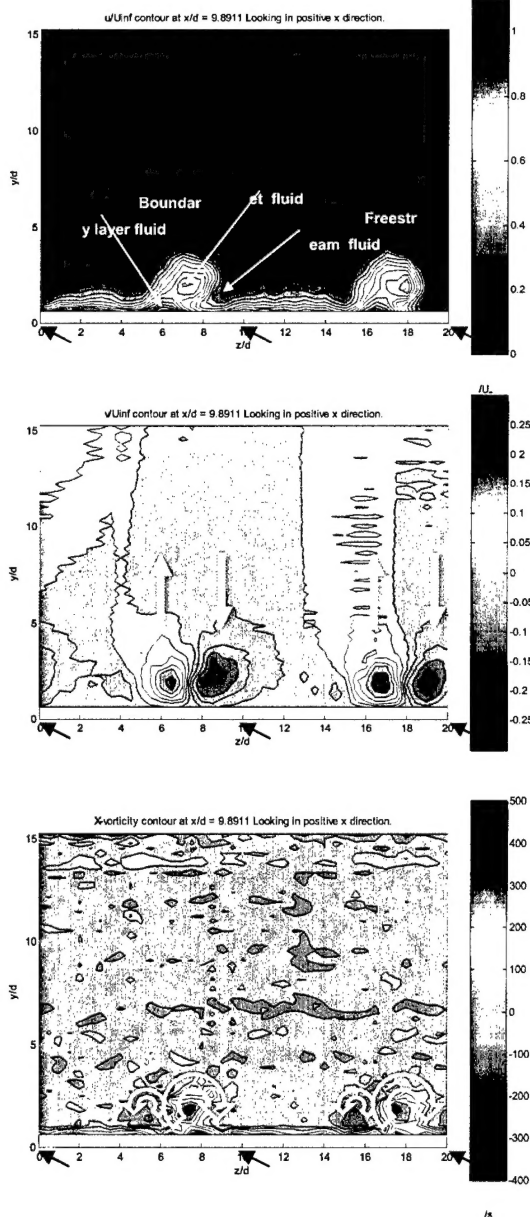


Figure 11: Streamwise and wall-normal velocity and out-of-plane (streamwise) vorticity contour maps showing angled VJ vortex development at  $x/d=10$ . Steady, angled jet injection into zero pressure gradient with  $B = 2$ .

As before, lobes of low  $u$ -velocity fluid indicate the presence of jet fluid, but it is clear that the trajectory of the angled jet is different from that of the normal jet. Because of the angle of injection, the jet fluid penetrates only half as far out from the wall as the normal jet, the center of the jet fluid reaching a maximum  $y/d$  of only 2.25 at  $x/d=20$ . There is, however, considerable migration in the spanwise direction, as the jet fluid travels to a position over 3 diameters in  $z$  from the injection point (Figure 12).

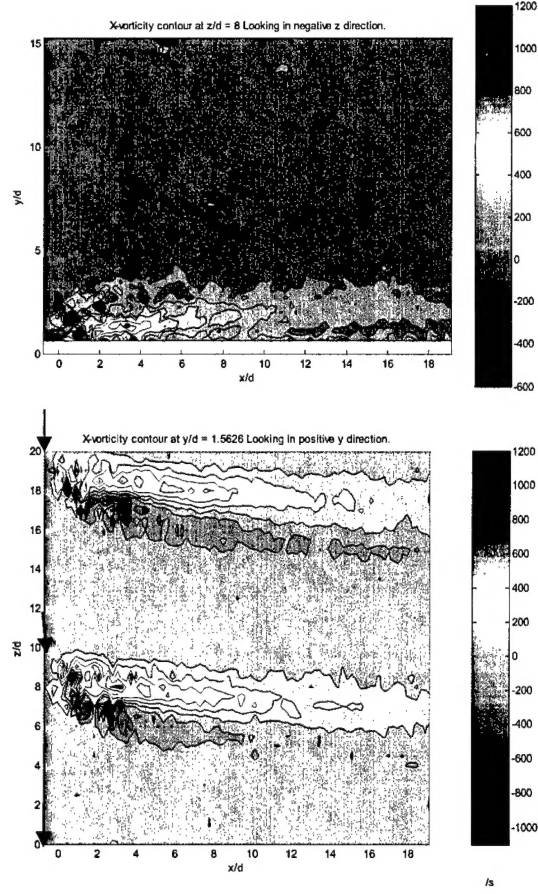


Figure 12: Streamwise vorticity contours shown in the  $xy$  (at  $z/d=8$ ) and  $xz$  (at  $y/d=1.5$ ) planes. Steady, angled jet injection into zero pressure gradient with  $B = 2$ .

The development of streamwise vortices is also apparent from Figures 11 and 12. The angled jet creates a double vortex, with the dominant positive vortex becoming much stronger and larger than the negative vortex. It is clear that the vortex caused by the angled jets migrates significantly in the spanwise direction, as fluid is forced out from the wall at  $2.5 z/d$  from the injection point and then circulates

back towards the wall. As in the case of normal injection, the vortex grows in size as it travels downstream. However, the primary vortex caused by the angled jets is a coherent structure for a longer distance. At a distance of 15 diameters downstream, the magnitude of the vorticity is reduced by only 45% (Figure 12).

Another phenomenon of interest is displayed more clearly in a three-dimensional plot of the flow field. Figure 13 shows the surface where the  $u$ -velocity component is 60% of the freestream velocity ( $u/U_\infty=0.6$ ). It is generated by traversing the 3D space of velocity data in the negative  $y$  direction from the freestream to the wall. The surface is then identified as the first occurrence of  $u/U_\infty=0.6$ . The jet injection location is indicated by arrows along the  $z$  axis, and the ensuing vortical effect is evident as the flow travels downstream. The plot is colored by surface height in the  $y$  direction.

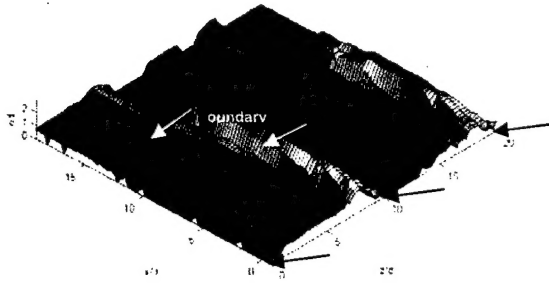


Figure 13: 3-D surface of streamwise velocity where  $u=0.6U_\infty$ . Steady, angled jet injection into zero pressure gradient with  $B = 2$ .

The dominant characteristic of Figure 13 is the double hump-like feature that develops downstream of each jet exit. The larger of the humps is the low-velocity jet fluid. After the fluid exits the hole, obstructing the freestream flow, it is gradually entrained by the main flow. By  $x/d=14$ , the lobe of jet fluid has been accelerated to above 60%  $U_\infty$ , and its presence in the surface contour in Figure 13 disappears.

A second low-velocity hump located closer to the wall extends farther in the  $x$  direction. This is indicative of boundary layer fluid being drawn out from the wall. The streamwise vortices caused by the angled jets occur sufficiently close to the wall that they pull low momentum fluid up from the boundary layer. This behavior is also evident in Figure 11, where a small pocket of low velocity fluid can be seen rising up from the wall at the position where the vortex has its highest outward movement ( $z/d \approx 6.5$ ). Likewise, the return motion of the cycling vortex brings high momentum freestream fluid back down close to the wall on the other side (at  $z/d \approx 8.5$ ).

#### Flat Plate, No Streamwise Pressure Gradient, Pulsed Jets

The effect of pulsed, angled jets was also investigated. A high pressure air line was connected to a Parker-Hannifin pulsed valve to create a pulsed jet of air. The valve was operated at a frequency of 5 Hz with a duty cycle of 25%. This jet was fed into the plenum show in Figure 8 to produce modulated air through the five center jet holes only. At the valve discharge into the plenum, the air pulse is essentially a step-function. Some attenuation occurs in the plenum resulting in a slightly modified jet waveform as shown in Figure 14. This figure shows the jet hole exit blowing ratio time history as measured with a single-element hot-wire positioned at the jet exit (with no freestream flow). The peak value of  $B$  is 2.5 and the mean value is 0.75 for this case. PIV data was collected at six points within the jet period and over one hole pitch (from  $-7 \leq z/d \leq 3$ ). Again, forty phase-locked images were averaged at each location. The timing of these points is also shown in Figure 14, and was selected in order to obtain data during the beginning, middle, and end of the pulse, as well as during the time that the pulse was off.

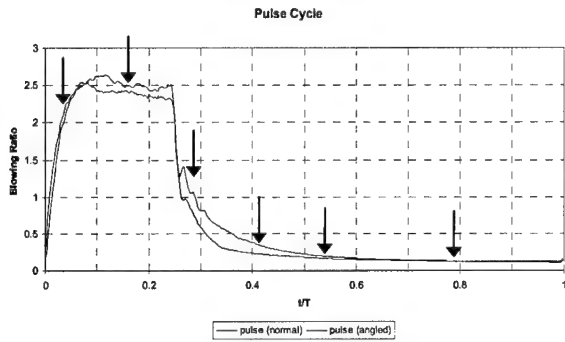


Figure 14: Jet hole exit blowing ratio time history for VGJ jet operation at 5Hz and 25% duty cycle. Arrows indicate PIV data collection points

As in the case of steady injection, vortices develop when the jets are pulsed. Evidence of this is shown in Figure 15, in which a contour map of the streamwise component of velocity is displayed, colored by height in  $y$  (similar to Figure 13). The surface represents the position at which  $u/U_\infty = 0.5$  and was taken during the second phase of the pulsing cycle (while the jet is on).

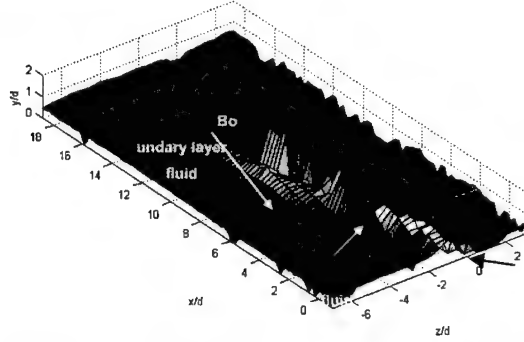


Figure 15: 3-D surface of streamwise velocity where  $u=0.5U_\infty$ . Data are taken during the "ON" portion of the pulsing cycle. Pulsed, angled injection into zero streamwise pressure gradient at 5Hz and 25% duty cycle with maximum  $B = 2.5$ . ( $t/T=0.165$ )

As in Figure 13, the jet fluid is clearly seen entering the flow field at the injection point. Likewise the second hump is seen at the left of the jet fluid, as the vortex sweeps the boundary layer fluid out from the wall during its rotation.

Figure 16 shows the change that the flow field experiences after the jet has been turned off (phase 4). The absence of jet fluid indicates that the jet fluid introduced into the flow during the "ON" portion of the pulsing cycle (as seen in Figure 15) has traveled downstream, and is no longer

visible in the data collection area. The vortex has also traveled farther downstream, however, the ensuing disruption in the boundary layer is still evident in the downstream portion of Figure 16.

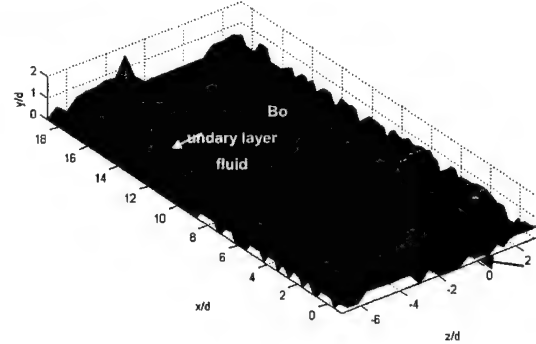


Figure 16: 3-D surface of streamwise velocity where  $u=0.5U_\infty$ . Data are taken during the "OFF" portion of the pulsing cycle. Pulsed, angled injection into zero streamwise pressure gradient at 5Hz and 25% duty cycle with maximum  $B = 2.5$  ( $t/T=0.415$ )

These results, both for the steady and pulsed jets, lend validity to the freestream entrainment theory for the angled jets. The structure and migration of the streamwise vortices indicate that high momentum freestream fluid is brought down close to the wall, effectively energizing the low momentum boundary layer. However, these observations are for a non-separating boundary layer. This leads to the following question: how does the previously discussed development of streamwise vortices affect boundary layer separation? The following section describes the efforts made to answer this question.

#### Flat Plate, Streamwise Pressure Gradient, Pulsed Jets

The test setup was modified in order to introduce both normal and angled pulsed jets into a separating boundary layer. The wedge shown in Figure 8 established a freestream velocity profile similar to that found on a Pak-B suction surface at a low Reynolds number. The wedge design is similar to that used by Volino and Hultgren, who documented its performance using a pressure coefficient ( $c_p$ ) based on the tunnel exit velocity:

$$c_p = 1 - \left( \frac{U_e}{U_{ex}} \right)^2 \quad (1)$$

Figure 17 shows a plot of this parameter vs. the streamwise distance ( $x$ ) normalized by the test section (suction surface) length ( $L_{ss}$ ), for the uncontrolled ( $B=0$ ) case compared to an ideal (unseparated) flow calculation. Data were taken with a single-element hot-wire at  $y/d = 7$  and midspan. The exit Reynolds number based on  $L_{ss}$  and  $U_{ex}$  for the wedge configuration is 90,000. This implies an equivalent inlet Reynolds number (based on  $C_x$  and  $U_{in}$ ) of 40,000 for the Pak-B blade profile. Using the same definition for dimensionless forcing frequency recommended in Bons et al. [ $F^+ = 0.41 f/(U_{in}/C_x)$ ], the  $F^+$  at 5Hz is 0.34.

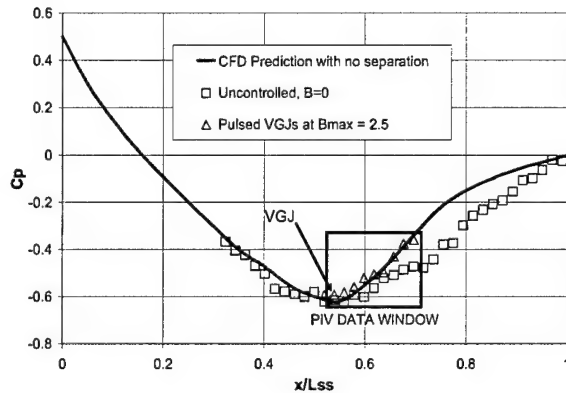


Figure 17:  $c_p$  distribution for wedge configuration showing uncontrolled and controlled pressure distribution in PIV data window.

The deviation in measured  $c_p$  from the ideal prediction for  $0.6 < x/L_{ss} < 1$  is indicative of boundary layer separation, since the desired flow deceleration is not achieved. Also shown in Figure 17 are the  $c_p$  measurements for pulsed VGJs, taken in the PIV data domain only. The correction of flow separation is evident.

The mainstream flow for the wedge configuration was modulated by a low frequency (0.9Hz) periodic unsteadiness of  $\pm 5\% U_i$  amplitude due to blower operation at low massflow. Since this frequency is roughly an order of magnitude lower than the convective throughflow frequency ( $U_{ex}/L_{ss}$ ) of the tunnel, it is expected that the boundary layer will respond in a quasi-steady manner. The influence of this unsteadiness on the results presented is currently under investigation.

PIV images were taken at 21  $z$  locations over one hole pitch for this low Reynolds number (separated) case. The boundary layer development for the uncontrolled cases ( $B=0$ ) is shown below in Figure 18, both for the flat plate (zero pressure gradient) and flat plate with the wedge inserted (applied streamwise pressure gradient).

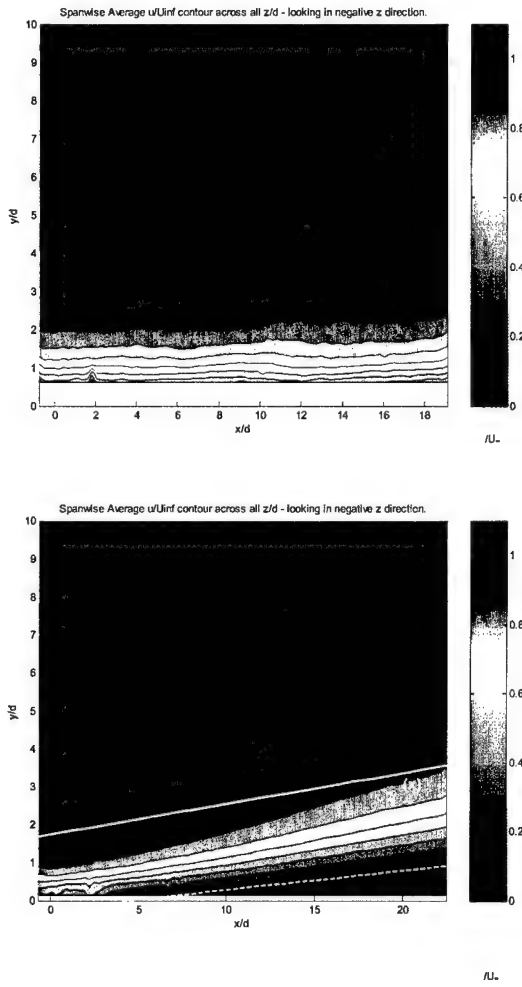


Figure 18: Spanwise averaged plots of the streamwise component of velocity for the uncontrolled ( $B=0$ ) cases: (a) no pressure gradient and (b) applied pressure gradient.

These contour plots are produced by averaging the  $x$ - $y$  planes at all 21  $z/d$  locations into a single plot. The effect of the presence of the inserted wedge is apparent in Figure 18. For the wedge case, the streamwise deceleration of the freestream flow produces a rapid increase in the boundary layer thickness and a near wall region of low momentum (separated) fluid (note dashed white line at  $u/U_{\infty} = 0.2$ ). By comparison, the boundary layer for the no-wedge flow

shows little perceptible streamwise development. The difference in the  $x/d=0$  boundary layer thickness between the two plots is due to the rapid acceleration upstream of the VGJ location in the wedge configuration.

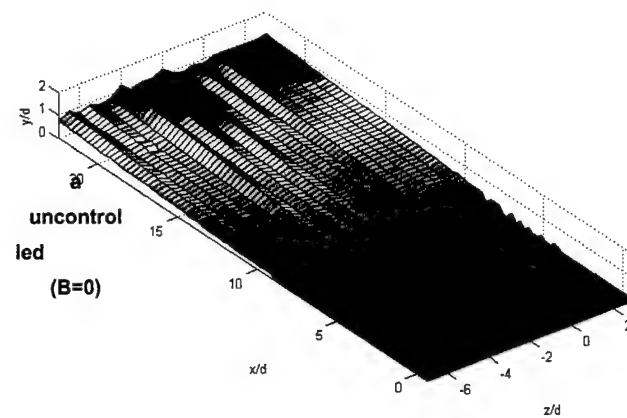
The results of the pulsed jet tests are displayed in Figure 19, for both normal (left column) and angled (right column) injection. The flow field is plotted as a three dimensional surface representing the position where  $u/U_\infty=0.2$ . It is expected that mean velocities below this magnitude are likely to indicate regions of unsteady flow separation. The uncontrolled case is shown first (Figure 19a) followed by the respective flow fields for the six phases within the pulsing cycle (Figure 19b-g).

For the uncontrolled flow, the separation zone (as denoted by the elevation of the  $u/U_\infty=0.2$  surface) begins about 8 diameters downstream of the jet injection point and grows to a maximum thickness of about  $y/d=1$  at  $x/d=20$ .

Figures 19b-g clearly display the disturbance caused by the jet and its effect on the boundary layer throughout the pulsing cycle. The jet hole location is indicated by the black arrow and the approximate extent of the injected fluid is marked with a pink oval. At the start of the angled jet pulse (Figure 19b), the separated area is already significantly smaller than the uncontrolled case, as the start is delayed farther downstream and its thickness is decreased.

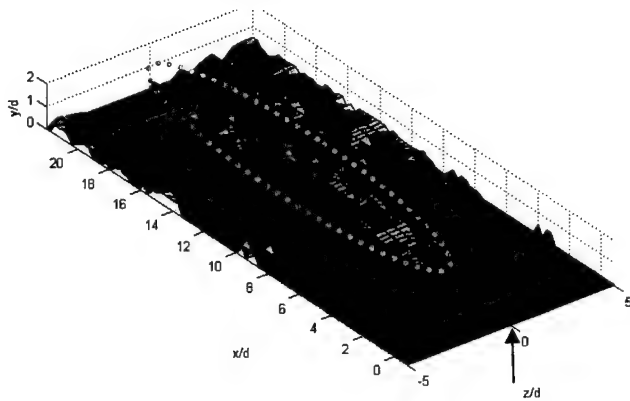
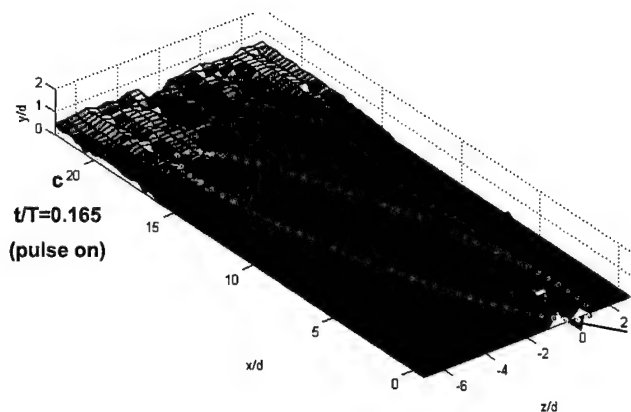
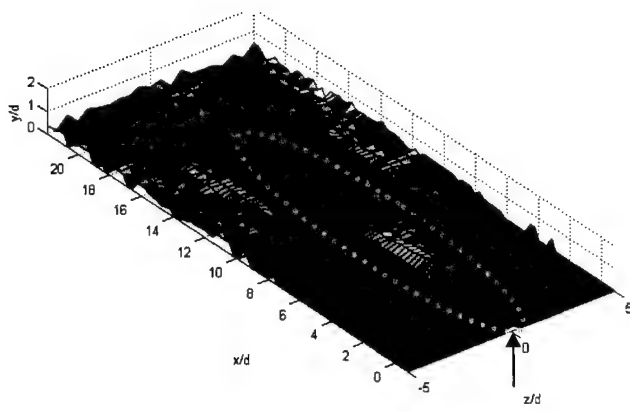
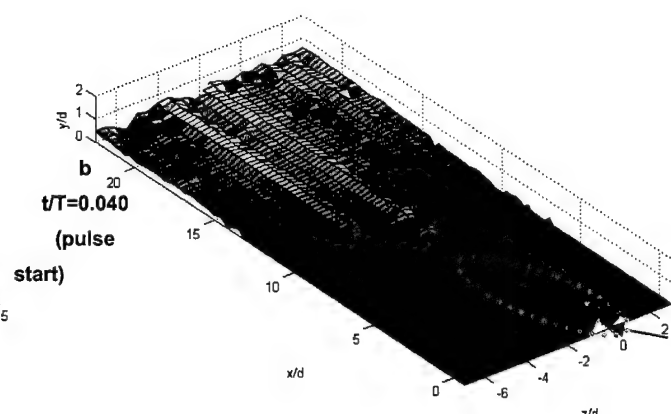
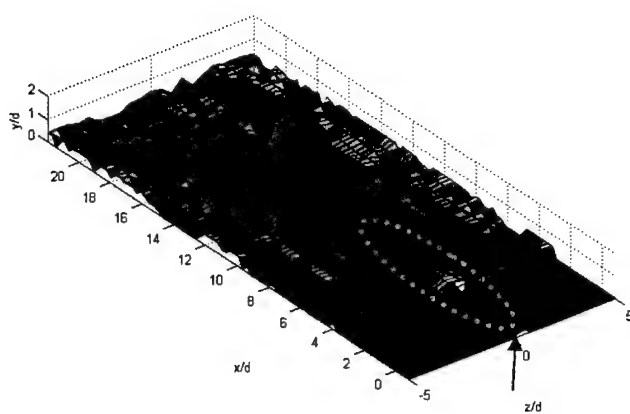
When the pulse is turned on, low streamwise momentum jet fluid is shown entering at  $x/d=0$ . The separated area begins about 10 diameters downstream of the jet injection point, growing to a maximum thickness of about  $y/d=0.5$  at the maximum downstream end of the figure. The separated area is already significantly smaller than the uncontrolled case. Nevertheless, it represents the maximum extent reached by the separation zone before the next pulse traverses the figure, effectively reenergizing the boundary layer. This reduction in size of the separated zone proceeds through the remainder of the pulse (Figure 19c) before almost completely disappearing (Figure 19d&e). It is not until the last two phases (Figure 19e&f) that the separation area begins to grow again, though it never quite reaches the uncontrolled state. The next pulsing cycle begins before the flow field can return to the uncontrolled condition.

The normal jets also produce similar boundary layer behavior. The jet pulse is turned on (Figure 19b), causing the separated zone to be pushed farther downstream and pulled in towards the wall, as in the case of the angled jets. After the pulse is turned off (Figure 19d&e) the separated zone continues to reduce in size before growing again in the final two phases (Figure 19e&f). As before the flow field does not recover the uncontrolled state even in the final phase. There is evidently much less spanwise uniformity in the separation zone in this case. This result will be discussed in more detail later.

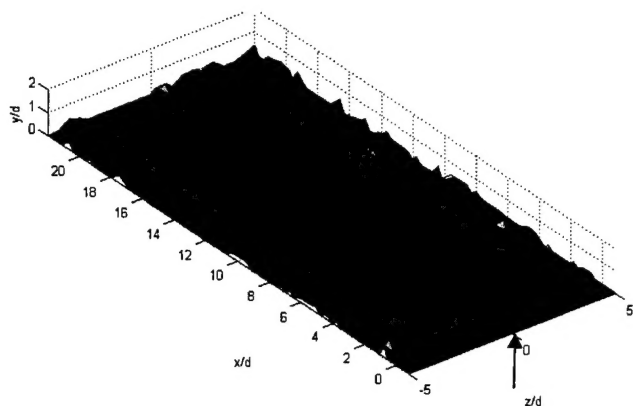


*Normal Injection*

*Angled Injection*



**Normal Injection**



**Angled Injection**

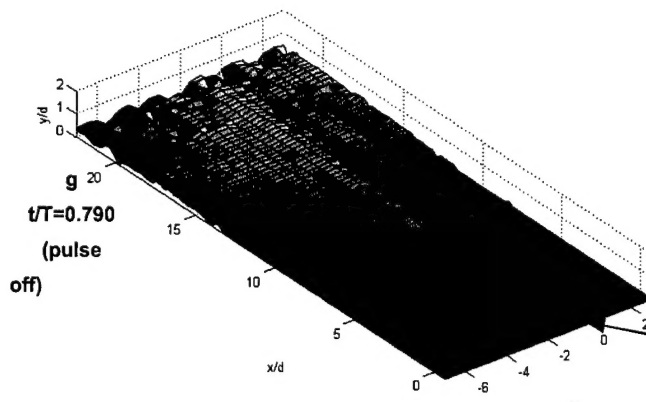
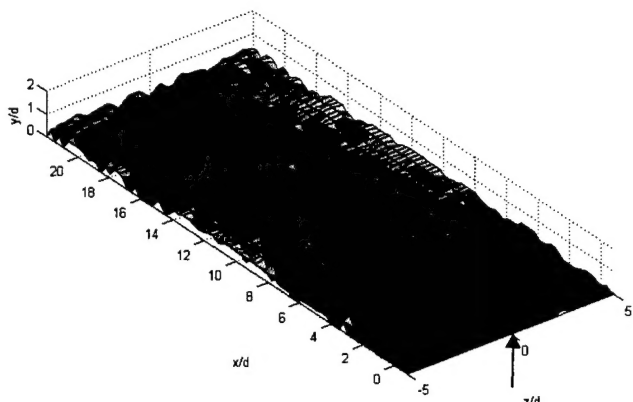
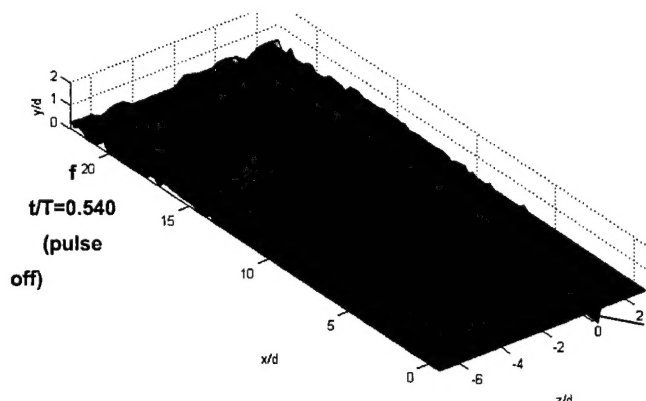
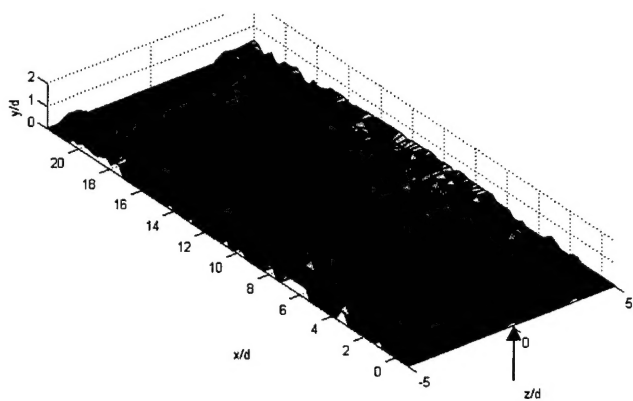
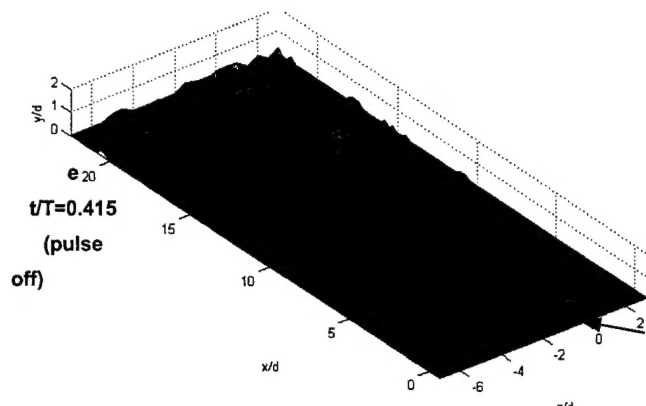


Figure 19. Spanwise averaged streamwise velocity contours for normal (left) and angled (right) jets. Black arrows indicate jet injection points. The pink ovals represent the position of the jet fluid.

In order to measure the effectiveness of VGJs, it is important to quantify the contribution of the boundary layer to separation losses in the flow field. Previous researchers have done this using the integrated total pressure measurements across the wake of the turbine blade<sup>5</sup>. Since the current flat plate testing facility has no blade wake, a boundary layer parameter comparable to the integrated wake pressure loss coefficient,  $\phi$  (Eq. 2), was evaluated.

$$\phi = \int_{mid-passage} \frac{P_{tot,i} - P_{tot,w}}{P_{tot,i} - P_{s,i}} dy \quad (2)$$

If the static pressure is assumed to be constant across the boundary layer and the total pressure in the free stream ( $y > \delta$ ) is constant,  $\phi$  can be written as  $\Gamma$ , Eq. 3, for low speed (incompressible), steady flow. This modified version of the integrated wake loss coefficient is referred to in this study as the integrated boundary layer momentum flux loss coefficient.

$$\Gamma = \int_0^{\delta} \frac{u_e^2 - u^2}{u_i^2} dy \quad (3)$$

For each phase of the pulsing cycle, this loss coefficient was calculated, time averaged, and then normalized by  $\Gamma_0$  (the loss coefficient of the uncontrolled case) (see Figure 20). The pulsing cycle is also shown at the bottom of the figure for ease of comparison. The calculation of  $\Gamma$  is performed at the trailing edge of the PIV data domain using the spanwise averaged streamwise velocity data (e.g. Figure 18).

A complication in the interpretation of Figure 20 is encountered because of the time lag of the flow disturbance. The loss coefficient is calculated from the data taken at the farthest downstream point of the flow field ( $x/d=20$ ). Therefore, this data does not correspond in time with the jet pulse shown in the figure. For example,

the loss coefficient calculated with the data taken during the first phase of the pulsing cycle is not indicative of the disturbance being caused at that moment by the initiation of the jet. Rather, it quantifies the losses associated with the preceding disturbance. Though the convective time of the disturbance is difficult to quantify precisely, it is roughly equivalent to  $T/5$ , or the distance between the 1<sup>st</sup> and 2<sup>nd</sup> data points in Figure 20. So, the effect of the pulse shown in the lower part of the figure appears at the trailing edge ( $x/d = 20$ ) roughly  $t/T = 0.2$  later.

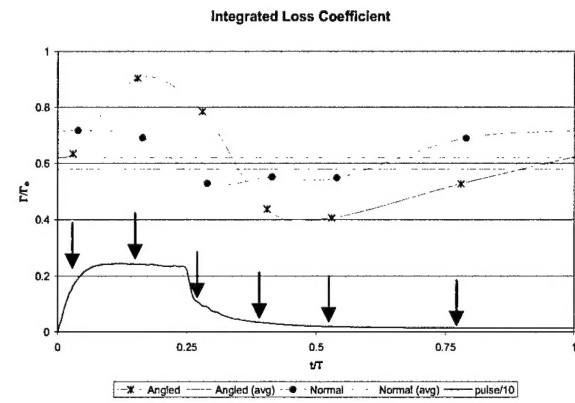


Figure 20: Integrated boundary layer momentum flux loss coefficient during the pulsing cycle. Normalized by the loss coefficient with  $B = 0$ . Pulsed injection into the wedge flow at 5 Hz and 25% duty cycle.

There are several observations that can be made from Figure 20. First, there appears to be very little difference in the cycle-averaged loss coefficient for both jet orientations; each has a value of about 0.6. Although the cycle-averaged loss coefficient for the angled jets is slightly lower than that calculated for the normal jets, the difference is slight, suggesting that neither orientation has a significant advantage over the other for these flow conditions.

Also of particular interest are the relative convection speeds of the disturbance. Figure 20 shows that the loss coefficient calculated from the angled jets is still increasing sharply when the flow control mechanism begins (between phases 1 and 2). The normal jets, however, show a modest drop in loss coefficient during the same phases. This suggests that

the effects of the normal jets travel more quickly than those caused by the angled jets. When the normal jet is turned on, the effects of the jet very quickly travel to the end of the data field, causing the drop in loss coefficient. The disturbance caused by the angled jet, however, takes longer to convect to the end of the flow field, and the decrease in loss coefficient occurs later. This behavior is reasonable when considered in terms of the migration of the jet vortices, as discussed earlier. The streamwise vortices created by the normal jets penetrated twice as far out from the wall as those caused by the angled jets. Thus, the normal vortices are carried out farther towards the higher velocity freestream flow. Meanwhile, the angled vortices remain closer to the wall and the low velocity boundary layer fluid, where they are convected downstream at a slower speed.

Although the normal jet flow control is carried downstream at a faster velocity, Figure 20 suggests that the angled jet flow control is of greater magnitude. This is seen by the depth of the decrease in loss coefficient. Between the second and fourth phases, the loss coefficient for the angled jets drops by 50%. In contrast, the normal jets only produce a 25% reduction in loss coefficient. This difference in effectiveness can be explained again by referencing the characteristics of the steady VGJs. The angled jets produced vortices of greater strength at a location closer to the wall, making them more effective at controlling the boundary layer separation. The vortices caused by the normal jets were weaker and located farther out from the wall, making it more difficult for the control effects of the vortices to reach the near-wall area.

The reason that the cycle-averaged losses for the angled and normal holes are roughly equivalent despite the more significant effect of the angled jets is clearly due to the higher separation losses registered during phase 2 of the PIV data. The value of  $\Gamma/\Gamma_0$  exceeds 0.9 for the angled jets at this point in the cycle. Figures 19b&c also show that separation is more extensive at its peak for the angled jets than for the normal jets. Though the mechanism

causing this effect is as yet unclear, it may be related to the residual hump of low momentum boundary layer fluid caused by the angled jet injection, as shown in Figures 15 and 16.

## CONCLUSIONS

The flat plate scenario was designed to give insight into the structure and movement of the vortical structures. Steady jets were injected normally and at an angle (30° pitch and 90° skew) to the freestream flow. The normal jet created a double vortex structure that grew in size while diminishing in strength as it traveled downstream. The vortices gradually migrated out from the wall, but maintained the same spanwise position. In contrast, the angled jet created a single vortex that migrated both up and out from the wall while remaining coherent for a longer distance than did the vortices generated by the normal jet. The vortices were observed to pull boundary layer fluid out from the wall and bring freestream fluid down close to the wall. This behavior was not as prominent when the jets were injected normally. These results show that the vortices produced by angled VGJs are structured in a way to more effectively promote freestream entrainment. Pulsed, angled jets were also applied to the flat plate flow. The results were comparable to the steady, angled jets. The lingering boundary layer effects caused by the streamwise vortices after the jet pulse had passed suggests that the flow control does not end immediately when the pulse is turned off.

The flat plate with an applied pressure gradient provided a separating boundary layer in which to test the effectiveness of pulsed VGJs. Normal and angled jets were again injected into the flow, and the reaction of the flow field was captured at six discrete points in the pulsing cycle. The integrated loss coefficient was calculated to provide a quantitative basis for comparison. It was found that the cycle averaged loss coefficient for both normal and angled jets was nearly equivalent. The normal jets produced a disturbance that traveled downstream more quickly, while the angled jets reduced boundary layer separation with greater magnitude.

## Bibliography

Bons, J.P. and Kerrebrock, J.L., 1999, "Complementary Velocity and Heat Transfer Measurements in a Rotating Cooling Passage with Smooth Walls," *ASME Journal of Turbomachinery*, Oct 1999, pp 651-662.

Bons, J., Sondergaard, R., and Rivir, R., 1999, "Control of Low-Pressure Turbine Separation Using Vortex Generator Jets", 37<sup>th</sup> Aerospace Sciences Meeting & Exhibit, Reno, Nevada. AIAA 99-0367, January 1999.

Bons, J., 2002, "Integrated Flow Control Devices (VGJs) for the Design of Enhanced Performance Low Pressure Turbines", proposal to AFOSR.

Eldredge, R.G. and Bons, J.P., 2004, "Active Control Of A Separating Boundary Layer With Steady Vortex Generating Jets - Detailed Flow Measurements," presented at the AIAA 42<sup>nd</sup> Aerospace Sciences Meeting and Exhibit in Reno, NV, 5-8 Jan 2004 (paper #AIAA 2004-0751).

Helton, D., 1997, private communication.

Matsunuma, T., Abe, H., Tsutsui, Y., and Murata, K., 1998, "Characteristics of an Annular Turbine Cascade at Low Reynolds Numbers.", presented at IGTI 1998 in Stockholm, Sweden, June 1998, paper #98-GT-518.

Matsunuma, T., Abe, H., and Tsutsui, Y., 1999, "Influence of Turbulence Intensity on Annular Turbine Stator Aerodynamics at Low Reynolds Numbers.", presented at IGTI 1999 in Indianapolis, Indiana, June 1999, paper #99-GT-151

Sharma et al., 1998, private communication.

Sondergaard, R., Bons, J., and Rivir, R., 2001, "Control of Low-Pressure Turbine Separation Using Vortex Generator Jets", *AIAA J. Propulsion and Power*, Vol. 18, No. 4, pp. 889-895. Jul/Aug 2002.

Sondergaard, R., Bons, J., Sucher, M., and Rivir, R., 2002, "Reducing LPT Stage Blade Count Using VGJ Separation Control." Presented at the 2002 International Gas Turbine Institute (IGTI) Conference in Amsterdam, The Netherlands, (paper #GT-2002-30602).

Volino, R. M. and Hultgren, L. S., "Measurements in Separated and Transitional Boundary Layers Under Low-Pressure Turbine Airfoil Conditions," *ASME Turbo Expo 2000*, 2000-GT-0260.